

Supporting Information

Chain-section engineering enables electron delocalization for efficient photocatalytic H₂O₂ synthesis in D-glucuronolactone-derived polymers

Yu Liu,^a Jiawei Lu,^a Shichen Cui,^a Haijiao Xie,^c Jianning He,^{*b} and Qingyao Wu^{*a}

^a College of Chemistry and Materials Science, Hebei University, The Flame Retardant Material and Processing Technology Engineering Research Center of Hebei Province, Baoding, Hebei, 071002, China.

^b College of Agronomy, Hebei Agricultural University, State Key Laboratory of North China Crop Improvement and Regulation, Key Laboratory of Crop Growth Regulation of Hebei Province, Baoding, Hebei, 071001, China.

^c Hangzhou Yanqu Information Technology Co., Ltd, Y2, 2nd Floor, Building 2, Xixi Legu Creative Pioneering Park, No. 712 Wen'er West Road, Xihu District, Hangzhou, Zhejiang, 310003, China.

*Correspondence: qyw@hbu.edu.cn ; 281579232@qq.com

Supplemental Experimental Details

Materials:

D-Glucuronic acid lactone (DG), 4,4'-Methylenedianiline (DMA), 4,4'-Thiodianiline (BS), 4,4'-Iminodianiline (NAB), and 4,4'-Oxydianiline (ODA) were purchased from Shanghai Aladdin Biochemical Technology Co., Ltd. Other solvents and reagents were purchased from local dealers. All chemicals and reagents were used directly without further purification.

Synthesis of DG-DMA:

Disperse 2 mmol of D-glucuronic acid lactone in a round-bottom flask comprising 20 mL of ethanol and heat to 60 °C. Upon dissolution, resulting in a transparent solution, introduce 2 mmol of 4,4'-Methylenedianiline and agitate at 60 °C for a duration of 5 hours. Upon completion of the reaction, permit the mixture to cool spontaneously to ambient temperature, recover the precipitate, and wash it to multiple rinses with deionized water and anhydrous ethanol to eliminate any lingering reactants and solvents attached to the solid surface. Dry the washed solid in an oven at 60 °C for 12 hours to facilitate drying. Upon drying, the desired product can be acquired.

Synthesis of DG-BS, DG-NAB and DG-ODA:

Similar to the synthesis of DG-DMA, while 4,4'-Thiodianiline, 4,4'-Iminodianiline and 4,4'-Oxydianiline were used instead of 4,4'-Methylenedianiline.

Characterizations:

To comprehensively characterize the polymer catalysts, a range of techniques were employed. Scanning electron microscope (SEM) images were obtained on the JSM-

7500. Transmission electron microscope (TEM) images were obtained on a ZEISS LSM 880 NLO with Airyscan. Fourier transform infrared (FT-IR) spectra were recorded on a Thermo Scientific Nicolet iS10 spectrometer. Solid-state ^{13}C nuclear magnetic resonance (NMR) spectra were obtained on a Bruker 400 M spectrometer. Powder X-ray diffraction (PXRD) patterns were measured by a Bruker D8 ADVANCE instrument with monochromatized Cu K α radiation operating at 40 kV and 40 mA. X-ray photoelectron spectroscopy (XPS) measurements were performed on the Thermo Scientific K-Alpha electron energy spectrometer with Al K α (1486.6 eV) radiation as the X-ray excitation source. UV-visible diffuse reflectance spectra (UV-vis DRS) were conducted on a Shimadzu UV-3600 instrument. Photoelectrochemical tests were performed on the CHI 760E workstation using a three-electrode system. Thermogravimetric analysis (TGA) was conducted using the integrated system of STA449C-QMS403C and the measurement of water contact angles was performed on the OCA-15EC device. The zeta potential of the catalysts was determined using the ZETASIZER NANO Series. UV-vis diffuse reflectance (DR) spectra were recorded on the T6 New Century ultraviolet-visible spectrophotometer using BaSO $_4$ as the reference, and the calibration curve and concentration of H $_2$ O $_2$ were measured. With the addition of DMPO, the free radicals produced in photocatalytic reaction were detected by electron paramagnetic resonance (EPR) on a Bruker EMX PLUS spectrometer.

Photoelectrochemical measurements:

Sample powders (5 mg) and Nafion (20 μ L) were homogeneously dispersed in ethanol (480 μ L) to prepare the stock solution. The as-obtained mixture was ultrasonically dispersed for 10 min. Subsequently, 100 μ L of the mixture was placed onto the ITO (1 \times 1 cm) and dried at room temperature. The measurements were conducted within a standard three-electrode setup, governed by the CHI 760E workstation. An Ag/AgCl electrode and a platinum sheet served as the reference and counter electrodes, respectively and the electrolyte employed was a 0.5 M Na₂SO₄ solution. Utilizing this setup, Electrochemical Impedance Spectroscopy (EIS) and Transient Photocurrent Response (TPR) curves were obtained. The transient photocurrent responses were recorded at a sampling interval of 20 seconds using a 60 W white LED lamp (PLS-LED 100C, Perfectlight, China). The Mott-Schottky analysis was conducted at modulation frequencies of 500 Hz, 1000 Hz, and 1500 Hz.

Rotating Disk Electrode (RDE) Analysis and Rotating Ring Disk Electrode (RRDE) Analysis :

The Rotating Disk Electrode test were carried out using a three-electrode system, where a rotating disk electrode (glassy carbon electrode with an area of 0.19625 cm²) was used as the working electrode. An Ag/AgCl electrode and a platinum sheet served as the reference and counter electrodes, respectively. Meanwhile, an O₂ saturated 0.1 M Phosphate buffer solution was used as the electrolyte (pH = 6.8). The working electrode was prepared as follows: 5 mg of catalyst powder was dispersed in a mixed solution of 480 μ L ethanol and 20 μ L Nafion, ultrasonicated for 30 minutes. Then, drop 10uL of the solution onto the glassy carbon rotating disk electrode and dry it at room

temperature. Linear sweep voltammograms (LSV) were obtained at room temperature with a scan rate of 10 mV s⁻¹ and at different rotation speeds ranging from 25² rpm to 45² rpm. The average electron transfer numbers (n) were calculated by the Koutecky-Levich equation:

$$\frac{1}{J} = \frac{1}{J_L} + \frac{1}{J_K} = \frac{1}{B \omega^{1/2}} + \frac{1}{J_K}$$

$$B = 0.2nFC_0D_0^{2/3}V^{-1/6}$$

Where J is the current density obtained by RDE measurements; J_L and J_K are the kinetic and diffusion current densities, respectively; ω is the angular velocity of the rotating speed; F is the Faraday constant (96485 C mol⁻¹); C_0 is the bulk concentration of O₂ (1.26 × 10⁻⁶ mol cm⁻³); D_0 is the diffusion coefficient of O₂ in 0.1 M phosphate buffer (2.7 × 10⁻⁵ cm² s⁻¹); and V is the kinetic viscosity of the electrolyte (0.01 cm² s⁻¹).

The Rotating Ring Disk Electrode test were carried out using a three-electrode system, where a glassy carbon disk with a platinum ring (RRDE. GCPT. S, Metrohm, electrode area: 0.1963 cm²) served as the working electrode. Continuously bubble nitrogen gas into the test solution for 30 minutes, keeping the rest of the conditions the same as with the rotating disk electrode. The rotation speed of the RRDE electrode was set to 1600 rpm. Set the potential of the ring electrode to -0.23 V (vs. Ag/AgCl) to detect O₂. Set the potential of the ring electrode to 0.6V (vs. Ag/AgCl) to detect H₂O₂.

AQY measurements:

For AQY measurements, 30 mg of photocatalyst was dispersed in 30 mL of water and O₂ was introduced into the solution until it was saturated. A 300 W Xe-lamp with a

band-pass filter of 450 nm, 485 nm, 520 nm, 595 nm, or 630 nm was used as the incident light source. The light intensity was adjusted to be 6.9 mW cm⁻², 3.7 mW cm⁻², 3.8 mW cm⁻², 1.0 mW cm⁻² and 3.5 mW cm⁻², respectively. The irradiation area was controlled to be 8.04 cm². The amount of H₂O₂ production was analyzed after 1 h irradiation. AQY was calculated using the following equation:

$$AQY(\%) = \frac{2N_{H_2O_2}}{\text{Number of incident photons}} \times 100\%$$

$$= \frac{(n_{H_2O_2} \times N_A \times h \times c) \times 2}{I \times S \times t \times \lambda} \times 100\%$$

where $N_{H_2O_2}$ was the amount of H₂O₂ production, N_A was the Avogadro constant (6.022×10^{23} mol⁻¹), h was the Planck constant (6.626×10^{-34} J·s), c was the speed of light (3×10^8 m·s⁻¹), S was the irradiation area (cm²), I was the irradiation intensity (W·cm⁻²), t was the irradiation time (s) and λ was the wavelength of incident light (m).

Solar-to-chemical conversion (SCC) efficiency:

The photocatalyst (40 mg) was added to water (40 mL) in a sample vial (45 mL). Then ultrasonicated for 10 min to disperse the photocatalyst and bubbled with O₂ for 10 min. The irradiation area was calculated to be 8.04 cm², with a light intensity of 45 mW cm⁻². The solar-to-chemistry conversion (SCC) efficiency was calculated using the following equation:

$$SCC(\%) = \frac{\Delta G \times N_{H_2O_2}}{P \times T} \times 100\%$$

Where ΔG is the free energy for H₂O₂ generation (117 kJ mol⁻¹); $N_{H_2O_2}$ is the yield of H₂O₂ (mol); P is the total input power (W); T is the photoreaction time (s).

Photosynthesis of H₂O₂:

The photocatalytic activity of the photocatalysts was evaluated using a multichannel photochemical reaction system (PCX-50C, Beijing Perfectlight Co., Ltd., China) equipped with a visible light source ($\lambda = 380\text{-}760\text{ nm}$). Typically, 2 mg of sample and 30 mL of ultrapure water were added into a glass bottle sealed with a rubber stopper. After ultrasound treatment to reach absorption desorption equilibrium, the suspension was stirred in the dark for 10 minutes with continuous O₂ as needed. The reaction temperature was maintained at 25 °C using a circulating water bath. After photocatalysis, the catalyst was removed with a 0.2 μm filter. 2mL of the filtered reaction solution was mixed with the same amount of barium sulfate solution and allowed to stand for five minutes. measure absorbance at 408 nm using UV-vis spectrophotometer, and calculate the concentration based on a standard curve.

To synthesize a titanium sulfate-sulfuric acid solution, 2 g of TiO₂ were combined with 200 mL concentrated sulfuric acid (98%) and subjected to heating at 150 °C for 20 hours. Subsequently, 10 mL this solution was introduced into 200 mL deionized water to yield a diluted titanium sulfate solution, which was then prepared for further analysis. 2 mL hydrogen peroxide at varying concentrations (0, 0.2, 0.4, 0.6, 0.8, and 1 mmol) were mixed with 2 mL aforementioned titanium sulfate solution within a centrifuge tube, allowing the reaction to proceed for a span of 5 minutes. The absorbance at a wavelength of 408 nanometers was quantified using a UV-vis spectrophotometer, thereby facilitating the establishment of a calibration curve (Fig. S10).

In experiments determining the optimal dosage for photocatalytic hydrogen peroxide production, 0.5-5 mg of DG-DMA catalyst was sequentially added to 30 mL of water, yielding Fig S11. Considering that weighing errors are significant at dosages of 0.5 mg or 1 mg, leading to unstable curves and large deviations in hydrogen peroxide yield calculations (expressed in $\mu\text{mol g}^{-1} \text{h}^{-1}$), a 2 mg catalyst dosage in 30 mL water was selected for subsequent reactions. Further, 2 mg aliquots of DG-DMA, DG-BS, DG-NAB, and DG-ODA were individually introduced into 30 mL water to generate Fig S12. All subsequent photocatalytic experiments were conducted using this dosage unless otherwise specified.

In-situ diffuse reflectance infrared Fourier transform spectroscopy (DRIFTS):

In-situ DRIFTS spectra were collected on a Nicolet iS 10 Fourier transform infrared spectrometer equipped with a mercury cadmium telluride detector. The reaction chambers used kHVC-DRP-5 (HARRICK) equipped with two KBr windows and one quartz window. The sample along with a Cu holder was put into the reaction chamber. Before the measurement, the sample was treated at 200 °C under N_2 (50 mL/min) to remove adsorbed contaminants on the catalysts. After the reaction chamber was cooled down to 298 K and the O_2 (20 mL/min) was put through H_2O vapor before sending into the reaction chamber. Collect the background after 30 minutes. The reactor was illuminated (0-60 min) with a 60 W white LED lamp (PLS-LED 100C, Perfectlight, China) to investigate the reaction process.

Theoretical calculation :

The computations were executed utilizing the Gaussian 16, C01 software suite. The M06-2X functional¹ was employed for the entirety of the calculations. Geometry optimization and frequency computations were conducted using the 6-31G (d, p) basis set,^{2,3} complemented by the integral-equation-formalism polarizable continuum model⁴ (IEF-PCM) for solvation in water. Singlet point energy calculations were executed with the 6-311G (d, p) basis set,⁵ and the Solvation Model Density (SMD)⁶ was utilized to incorporate the effects of water solvation. The HOMO/LUMO and ELF⁷ functions were assessed and visualized through the Multiwfn⁸ and VMD⁹ software applications.

Supporting data

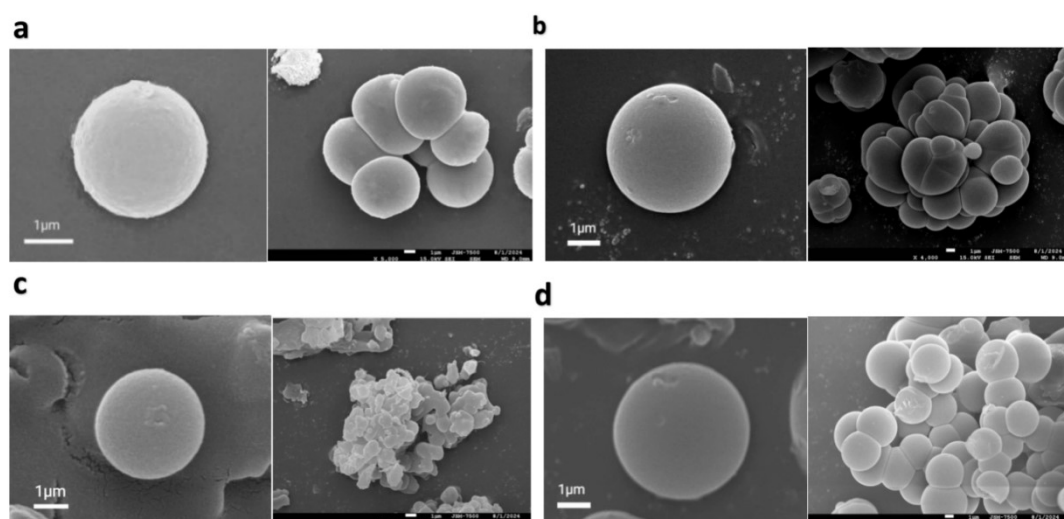


Fig. S1 SEM images of catalysts (a) DG-DMA, (b) DG-BS, (c) DG-NAB, and (d) DG-ODA.

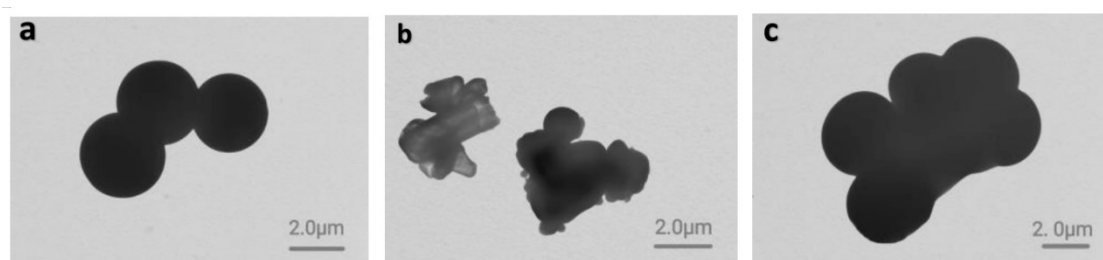


Fig. S2 TEM images of catalysts (a) DG-BS, (b) DG-NAB, and (c) DG-ODA.

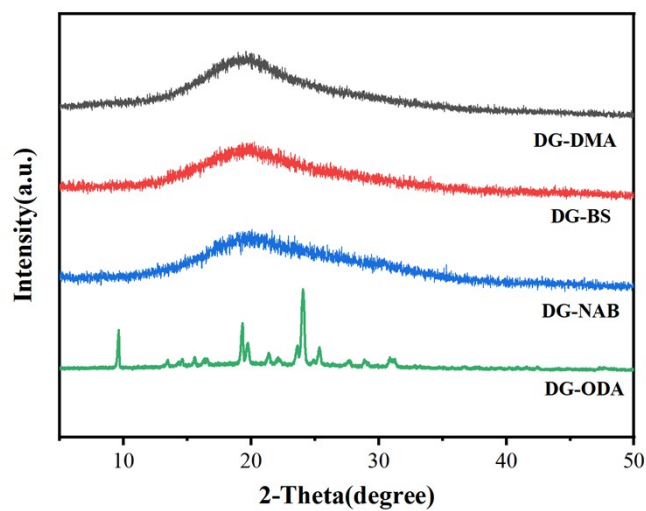


Fig. S3 Powder X-ray diffraction spectra of catalysts DG-DMA, DG-BS, DG-NAB, and DG-ODA.

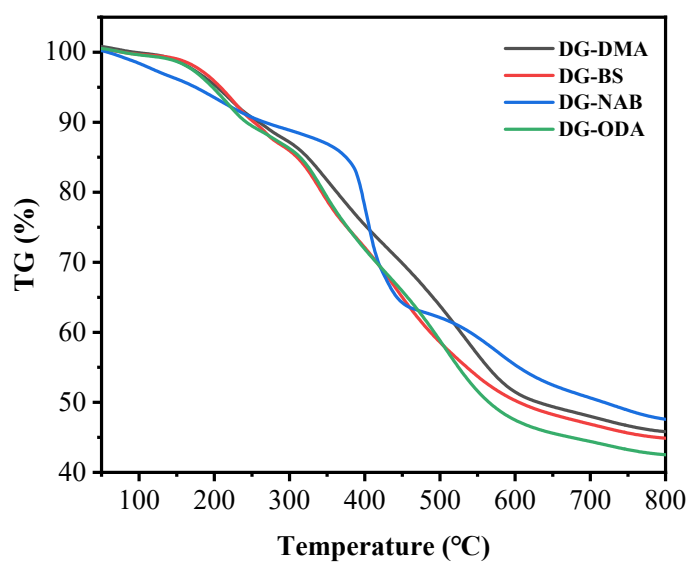


Fig. S4 Thermogravimetric plots of catalysts DG-DMA, DG-BS, DG-NAB and DG-ODA.

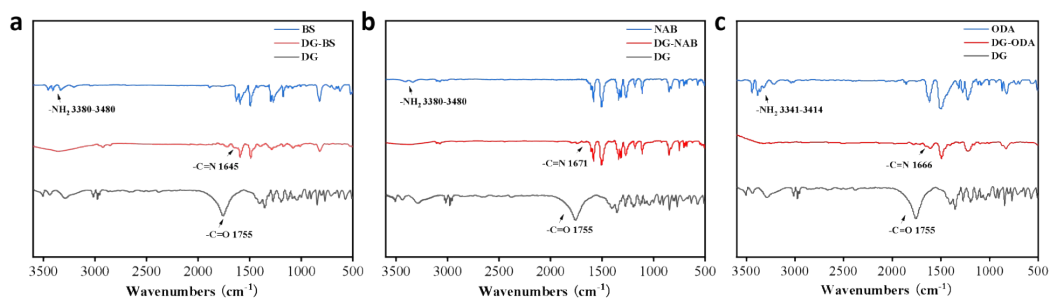


Fig. S5 FT-IR spectra of Catalysts (a) DG-BS, (b) DG-NAB, (c) DG-ODA and Corresponding Monomers.

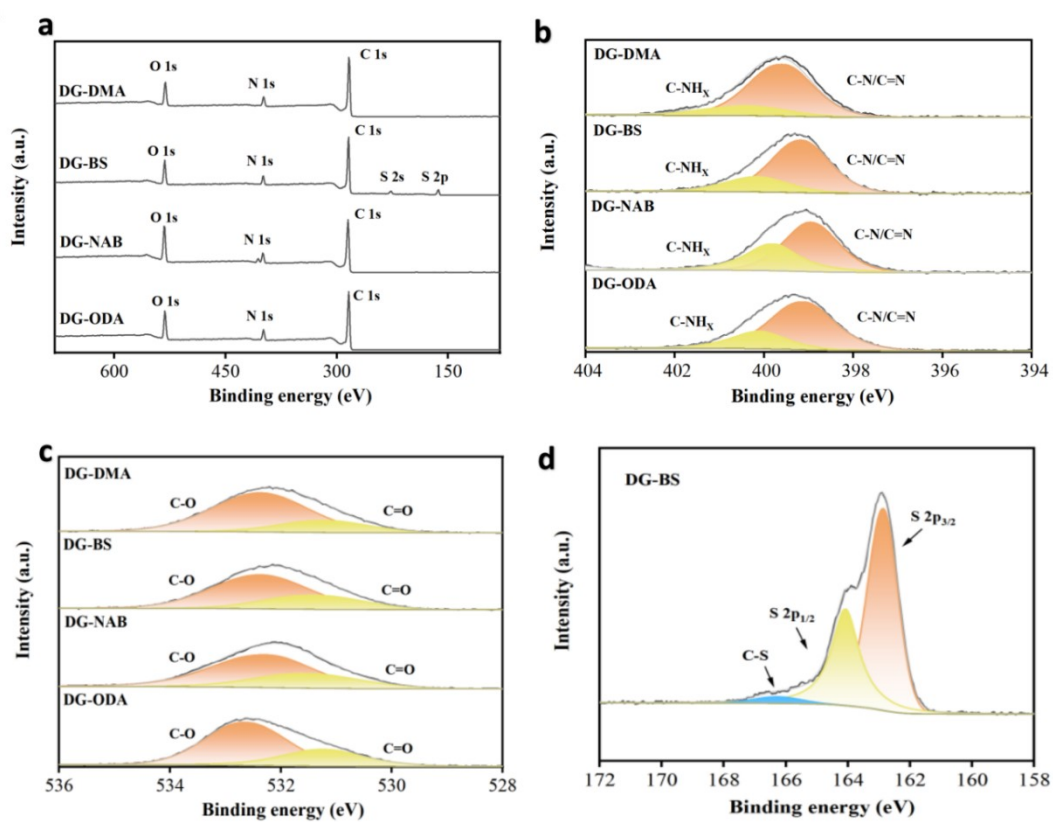


Fig. S6 X-ray photoelectron spectra of catalysts (a) survey spectra, (b) DG-BS, (c) DG-NAB, and (d) DG-ODA.

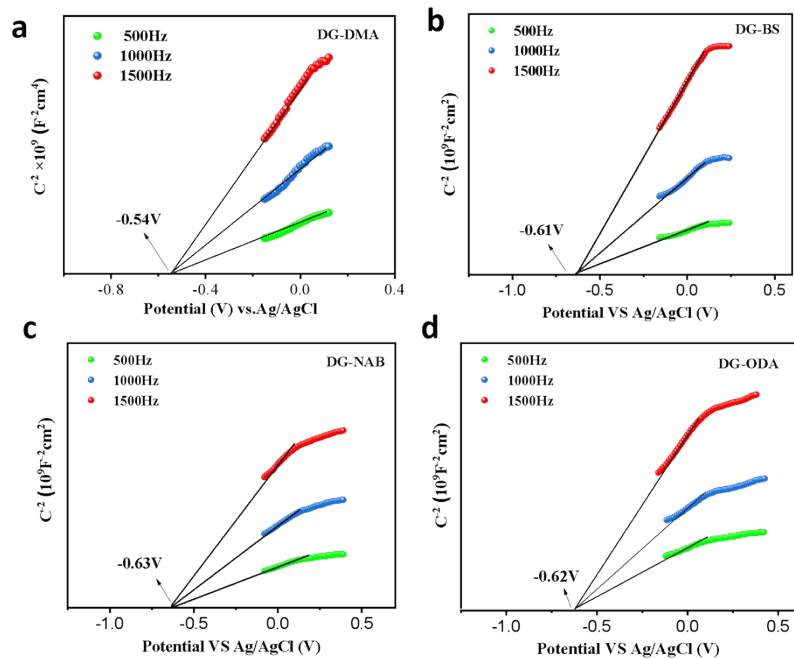


Fig. S7 Mott-Schottky curves of catalysts (a) DG-DMA, (b) DG-BS, (c) DG-NAB, and (d) DG-ODA.

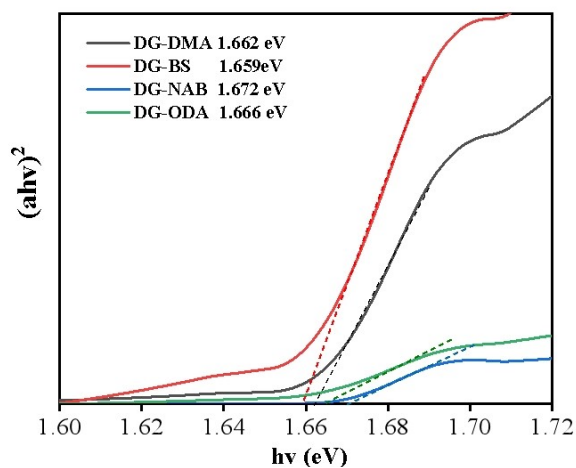


Fig. S8 Tauc plots of DG-DMA, DG-BS, DG-NAB, and DG-ODA.

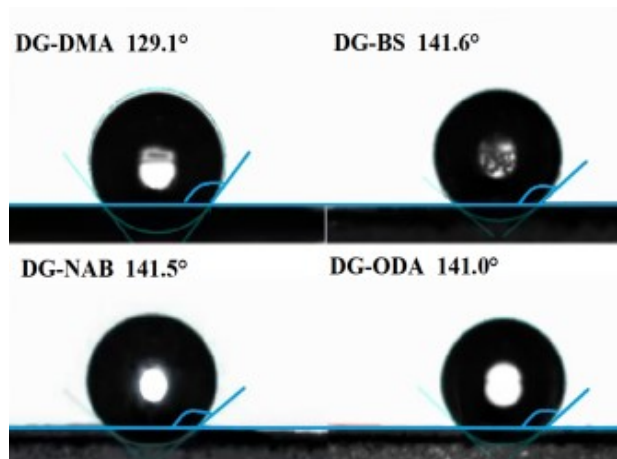


Fig. S9 Contact angle test of DG-DMA, DG-BS, DG-NAB, and DG-ODA.

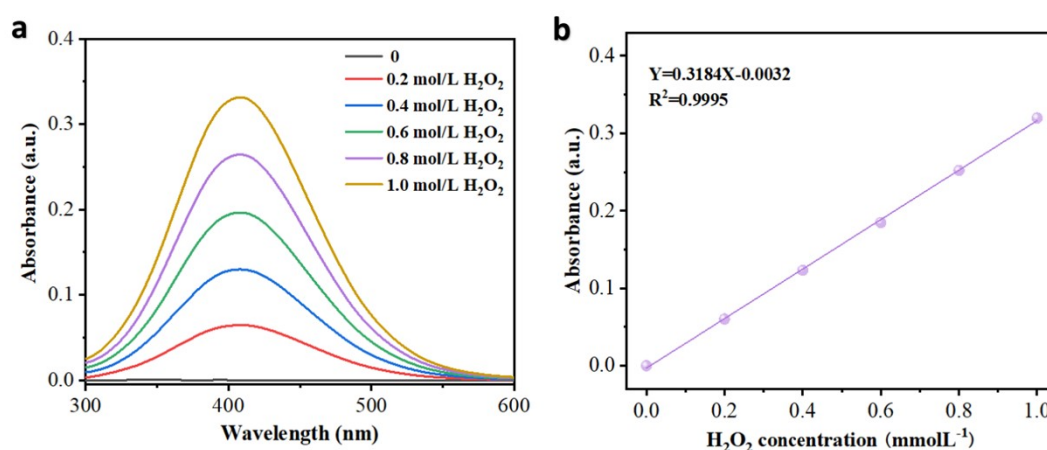


Fig. S10 (a) The absorbance of different concentrations of H₂O₂ standard solutions in the UV-visible spectrum was determined using a titanium sulfate solution method. (b) The linear fitting curve corresponding to the absorbance and H₂O₂ concentration.

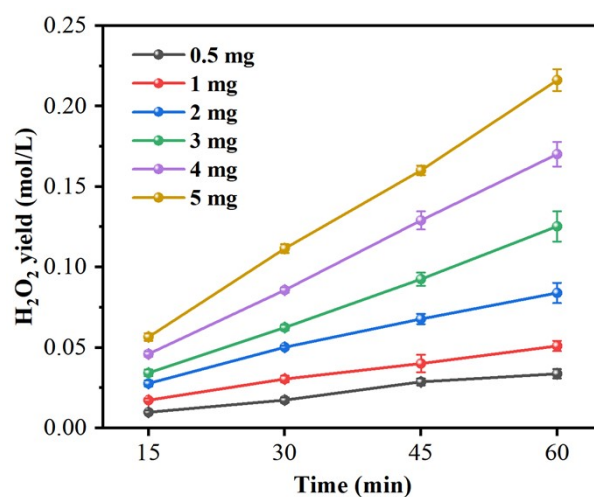


Fig. S11 Optimal dosage test of catalyst DG-DMA.

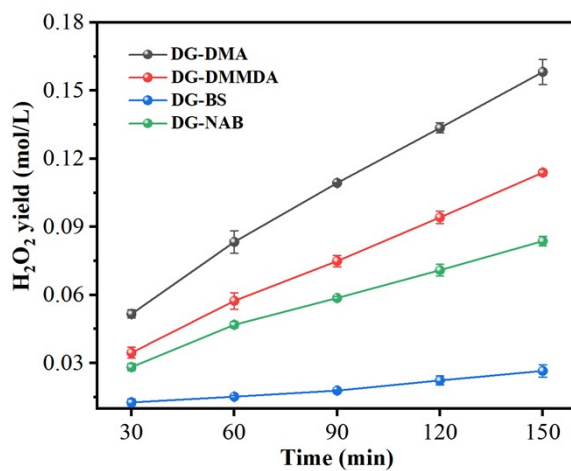


Fig. S12 Optimal dosage test for catalyst DG-DMA (2mg of each catalyst added to 30mL of water).

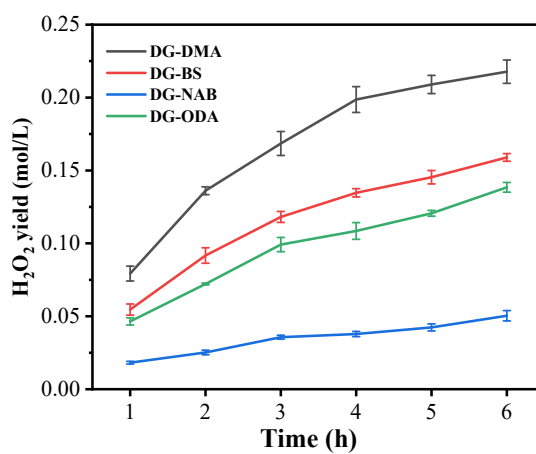


Fig. S13 Photocatalytic H₂O₂ production performances of catalyst upon 6 hours continuous visible light irradiation.

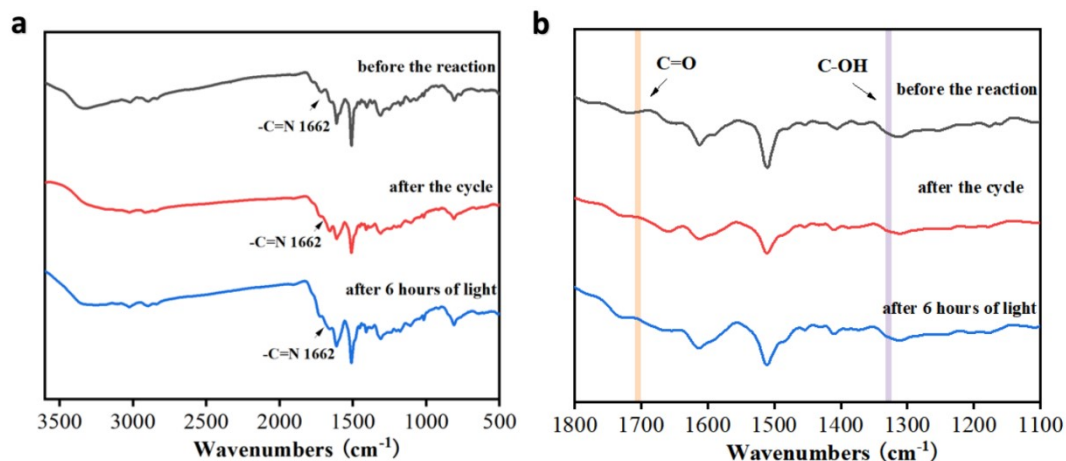


Fig. S14 (a) Infrared contrast images of catalyst DG-DMA before continuous illumination for six hours and cyclic reaction for eight times. (b) zoomed-in region of Fig S14a.

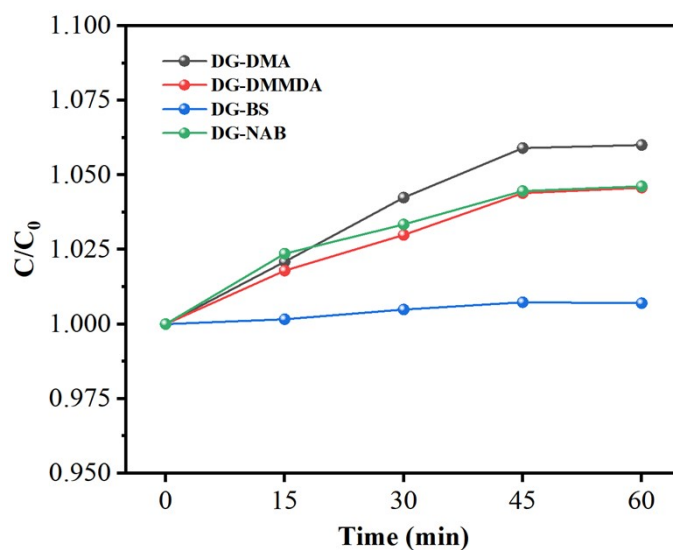


Fig. S15 Photocatalytic decomposition of H₂O₂ aqueous solution (C₀ = 1 mM) under visible light irradiation over DG-DMA, DG-BS, DG-NAB and DG-ODA.

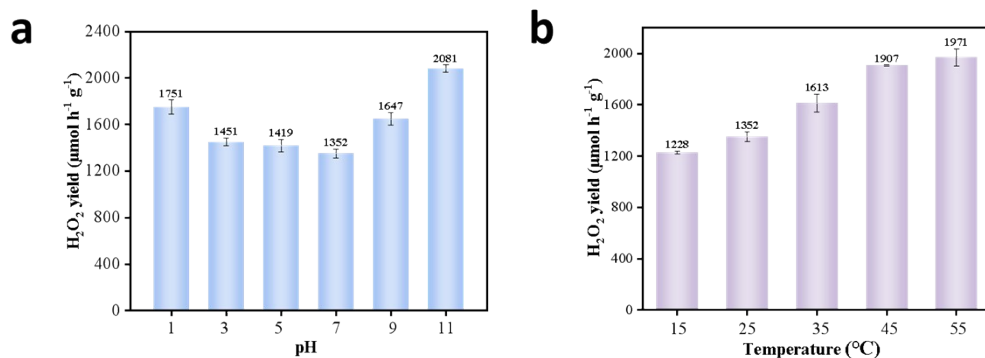


Fig. S16 H₂O₂ yield at (a) different pH conditions and (b) different temperature conditions for DG-DMA.

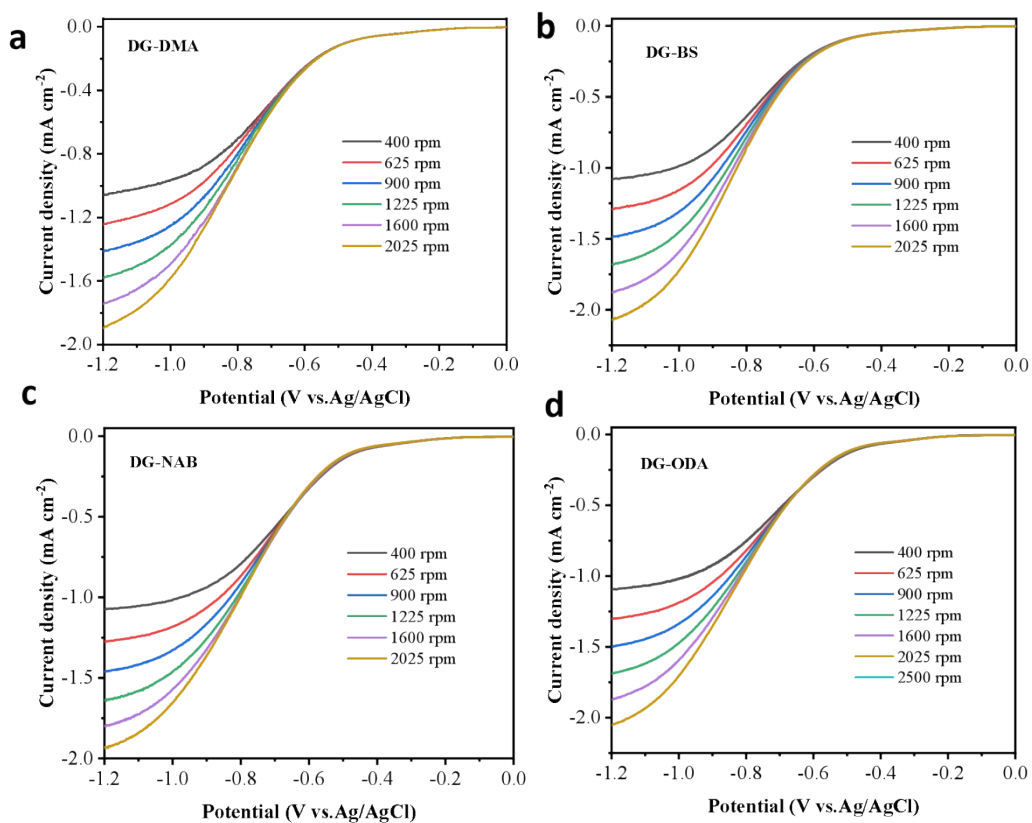


Fig. S17 Linear sweep voltammograms of catalysts (a) DG-DMA, (b) DG-BS, (c) DG-NAB, and (d) DG-ODA.

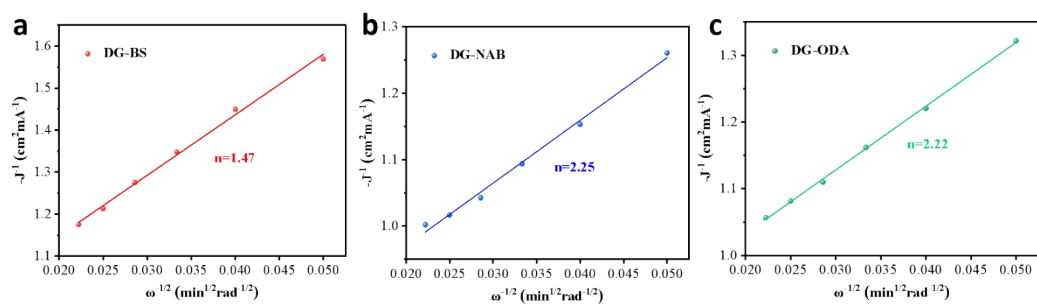


Fig. S18 Electron transfer number graph for catalysts (a) DG-BS, (b) DG-NAB, and (c) DG-ODA.

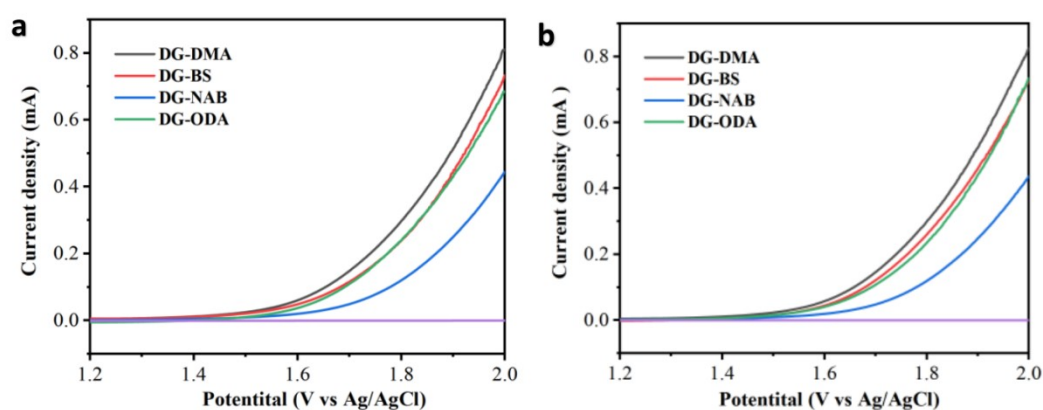


Fig. S19 Voltammograms of the catalysts DG-DMA, DG-BS, DG-NAB and DG-ODA at the rotating ring-disk electrode at potentials of (a) 0.6V, and (b) -0.23V.

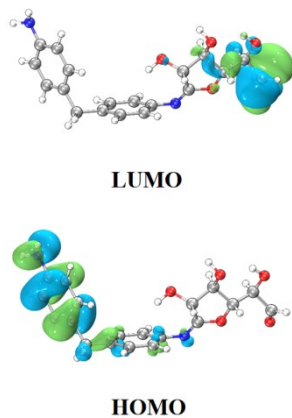


Fig. S20 The calculated HOMO and LUMO distributions of DG-DMA.

Table S1. The proportion of binding energies for catalysts DG-DMA, DG-BS, DG-NAB and DG-ODA.

Proportion (%)	DG-DMA	DG-BS	DG-NAB	DG-ODA
C=C/C-C	0.72	0.73	0.67	0.58
C-S/C-O	0.23	0.21	0.10	0.31
C=N/C-N	0.01	0.04	0.19	0.09
C=O	0.03	0.01	0.05	0.02

Table S2. Comparison of the photocatalytic H₂O₂ production performances among reported organic catalysts.

Photocatalyst	H ₂ O ₂ production rate ($\mu\text{mol g}^{-1} \text{h}^{-1}$)	Irradiation conditions	Dosage of Reaction solution and atmosphere	Reference
DG-DMA	1352	0.36 W (LED) $\lambda > 380 \text{ nm}$ 45 mW cm ⁻²	Water, Air	This work
	2696		NBA, Air	
	3453		NBA, O ₂	
RUT-4	1321	$\lambda > 420 \text{ nm}$ 81.6 mW cm ⁻²	Seawater, Air	10
	742		Water, Air	
PM-CDs-30	1776	0.28 W (LED) $\lambda \geq 420 \text{ nm}$ 34.8 mW cm ⁻²	Seawater, Air	11
	1340		Water, Air	
HTCC	1160	300 W (Xe) $\lambda \geq 420 \text{ nm}$	Water, Air	12
N, S-CDs	2062.4	AM 1.5 G $\lambda > 400 \text{ nm}$ 100 mW cm ⁻²	Water, Air	13
MRFS-7	600	300 W (Xe) $\lambda > 420 \text{ nm}$	Water, Air	14
CNOP	930	300 W Xe $\lambda > 420 \text{ nm}$ 350 mW cm ⁻²	Water, Air	15
CDA300	558	300 W (Xe) $\lambda > 420 \text{ nm}$	Water, Air	16
aMIL-3	926	300 W (Xe) $\lambda > 420 \text{ nm}$	TEOA, O ₂	17
DETH-COF	1000	300 W (Xe) $\lambda > 420 \text{ nm}$	Water, Air	18
1H-COF	1483	300 W (Xe) $\lambda > 420 \text{ nm}$	IPA, Air	19
G-HTC	480.7	300 W (LED) $\lambda > 420 \text{ nm}$ 100 mW cm ⁻²	Water, Air	20
COF-O	1500	30 W (LED) $\lambda = 420 \text{ nm}$ 10 mW cm ⁻²	Water, O ₂	21
DMCR-1NH	2588	300 W (Xe) $\lambda > 420 \text{ nm}$	IPA, O ₂	22

EBA-COF	1820	50 W (LED) $\lambda = 420 \text{ nm}$	EtOH, O ₂	23
CoPc-BTM-COF	2096	300 W (Xe) $\lambda > 400 \text{ nm}$	EtOH, O ₂	24
TF50-COF	1739	300 W (Xe) $\lambda > 400 \text{ nm}$ 8.33 mW cm ⁻²	EtOH, O ₂	25
PC-DM	1618	0.36 W (LED) $\lambda > 380 \text{ nm}$ 45 mW cm ⁻²	EtOH, O ₂	26

References:

1. Y. Zhao and D. G. Truhlar, *Theor. Chem. Acc.*, 2007, **119**.
2. R. Ditchfield, W. J. Hehre and J. A. Pople, *J. Chem. Phys.*, 1971, **54**, 724-728.
3. M. J. Frisch, J. A. Pople and J. S. Binkley, *J. Chem. Phys.*, 1984, **80**, 3265-3269.
4. G. Scalmani and M. J. Frisch, *J. Chem. Phys.*, 2010, **132**, 114110.
5. R. Krishnan, J. S. Binkley, R. Seeger and J. A. Pople, *J. Chem. Phys.*, 1980, **72**, 650-654.
6. A. V. Marenich, C. J. Cramer and D. G. Truhlar, *JPC B*, 2009, **113**, 6378-6396.
7. L. U. Tian and C. Fei-Wu, *Acta Phys.-Chim. Sin.*, 2011, **27**, 2786-2792.
8. T. Lu and F. Chen, *J Comput Chem*, 2012, **33**, 580-592.
9. W. Wriggers and K. Schulten, *Proteins:Struct., Funct., Genet.*, 1997, **29**, 1-14.
10. J. Wang, J. Li, Z. Li, J. Wu, H. Si, Y. Wu, Z. Guo, X. Wang, F. Liao, H. Huang, M. Shao, Y. Liu and Z. Kang, *Nano Res.*, 2024, **17** 5956-5964.
11. Q. Wu, J. Cao, X. Wang, Y. Liu, Y. Zhao, H. Wang, Y. Liu, H. Huang, F. Liao, M. Shao and Z. Kang, *Nat. Commun.*, 2021, **12**, 483.

12. L. Xu, Y. Liu, L. Li, Z. Hu and J. C. Yu, *ACS Catal.*, 2021, **11**, 14480-14488.
13. H. Qin, K. Sun, P. Hao, H. Yuan, Y. Shen, A. Bian, Y. Cui, J. Hou, W. Shi, C. Li and F. Guo, *J. Catal.*, 2024, **435**, 115579.
14. Q. Tian, L. Jing, S. Ye, J. Liu, R. Chen, C.-A. H. Price, F. Fan and J. Liu, *Small*, 2021, **17**, e2103224.
15. K. Hyejin, S. Kyuin, L. Kyoung, H. Jeong, Z. Yongfa and C. Won, *Appl. Catal. B Environ.*, 2021, **299**, 120666.
16. C. Cheng, L. Qiu, M. Wei, Q. Hehe, L. Xin, Y. Du and M. Shun, *Appl. Catal. B Environ.*, 2022, **314**, 121485.
17. J. Xue, W. Yao, L. Yun, S. Ke, Y. Meng and T. Jun, *Nano Res.*, 2022, **15**, 6045-6053.
18. G. Pan, X. Hou, Z. Liu, C. Yang, J. Long, G. Huang, J. Bi, Y. Yu and L. Li, *ACS Catal.*, 2022, **12**, 14911-14917.
19. H. Hu, Y. Tao, D. Wang, C. Li, Q. Jiang, Y. Shi, J. Wang, J. Qin, S. Zhou and Y. Kong, *J. Colloid Interface Sci.*, 2022, **629**, 750-762.
20. W. Miao, D. Yao, C. Chu, Y. Liu, Q. Huang, S. Mao and K. Ostrikov, *Appl. Catal. B Environ.*, 2023, **332**, 122770.
21. Z. Xie, X. Chen, W. Wang, X. Ke, X. Zhang, S. Wang, X. Wu, J. C. Yu and X. Wang, *Angew. Chem., Int. Ed.*, 2024, **136**, e202410179.
22. P. Das, G. Chakraborty, J. Roeser, S. Vogl, J. Rabeah and A. Thomas, *J. Am. Chem. Soc.*, 2023, **145**, 2975-2984.

23. L. Zhai, Z. Xie, C. Cui, X. Yang, Q. Xu, X. Ke, M. Liu, L. Qu, X. Chen and L. Mi, *Chem. Mater.*, 2022, **34**, 5232-5240.
24. Q. Zhi, W. Liu, R. Jiang, X. Zhan, Y. Jin, X. Chen, X. Yang, K. Wang, W. Cao, D. Qi and J. Jiang, *J. Am. Chem. Soc.*, 2022, **144**, 21328-21336.
25. H. Wang, C. Yang, F. Chen, G. Zheng and Q. Han, *Angew. Chem., Int. Ed.*, 2022, **133**, 1-6.
26. Y. Li, Y. Liu, J. Lu, L. Yang, H. Xie, J. He and Q. Wu, *ACS Appl. Polym. Mater.*, 2025, **7**, 6909-6919.